

Exposing {001} Crystal Plane on Hexagonal Ni-MOF with Surface-Grown Cross-Linked Mesh-Structures for Electrochemical Energy Storage

Yan Li, Yuxia Xu, Yong Liu, and Huan Pang*

Hexagonal nickel-organic framework (Ni-MOF) [Ni(NO₃)₂·6H₂O, 1,3,5-benzenetricarboxylic acid, 4-4'-bipyridine] is fabricated through a one-step solvothermal method. The {001} crystal plane is exposed to the largest hexagonal surface, which is an ideal structure for electron transport and ion diffusion. Compared with the surrounding rectangular crystal surface, the ion diffusion length through the {001} crystal plane is the shortest. In addition, the cross-linked porous mesh structures growing on the {001} crystal plane strengthen the mixing with conductive carbon, inducing preferable conductivity, as well as increasing the area of ion contact and the number of active sites. These advantages enable the hexagonal Ni-MOF to exhibit excellent electrochemical performance as supercapacitor electrode materials. In a three-electrode cell, specific capacitance of hexagonal Ni-MOF in the 3.0 M KOH electrolyte is 977.04 F g⁻¹ and remains at the initial value of 92.34% after 5,000 cycles. When the hexagonal Ni-MOF and activated carbon are assembled into aqueous devices, the electrochemical performance remains effective.

it has been found that the organic template can guide the nucleation and growth of inorganic nanocrystals by artificial modification or synthesis to obtain the ideal shape, size, and final properties.^[3,4] Metal-organic framework (MOF), a new type of porous crystalline material, is composed of two main components: inorganic vertices (metal ions or clusters) and organic linkers.^[5,6] By varying metal ions and organic ligands, over 20 000 varied MOFs have been reported, and their structures are not only abundant but also designable.^[7,8] In addition to their various structures and compositions, MOF has high surface areas, large pore volumes, and uniform pore dispersions compared to conventional microporous and mesoporous materials (zeolite, mesoporous SiO₂, and activated carbon (AC)).^[9-11] These inherent characteristics make MOF very promising in a variety

1. Introduction

Nanocrystals possess multifarious size and shape-related characteristics for a variety of fields including electronics, catalysis, and optics.^[1,2] Owing to the characteristics of nanocrystal growth kinetics, yet synthesis process often needs rigorous experimental conditions, and nanocrystals are difficult to control in size and shape. In addition, additives like ligands and metal ions are required on many occasions. In recent years,

of applications including gas adsorption and separation,^[12,13] catalysis^[14] Y, drug delivery,^[15] proton conductivity and sensing.^[16] Furthermore, several MOFs have been investigated for various electrochemical applications, such as supercapacitors, batteries, and fuel cells.^[17-19]

Supercapacitors (SCs), as a key enabling electrical energy storage technology, have drawn continuing attention because of their superior power densities, charge-discharge rates, and longer cycling lives than secondary batteries.^[20,21] It is well known that the electrochemical properties of electrochemical energy storage devices mainly depend on the electrode materials. According to the working mechanism of supercapacitors, electrode materials are classified into carbon materials^[22] (electric-double-layer capacitors) and pseudocapacitor electrode materials including metal sulfide,^[23] metal oxides,^[24] metal selenide,^[25] metal hydroxide,^[26] conductive polymers,^[27] and so on, which mainly store energy by reversible redox reactions. Recently, rapidly growing MOF materials have achieved extensive specific surface area, large pore volume, and uniform pore dispersions, which can provide potential electrode candidates for SCs.^[28] The supercapacitive application of MOF can be mainly classified into two types. One is to use MOF as a template to prepare MOF derivatives: metal oxides, metal nanoparticles, porous carbon compounds, etc.^[29,30] The other is that pure MOFs are directly applied to electrode materials for SCs and their capacitance are based on the reversible redox

Y. Li, Y. Xu, Prof. H. Pang
School of Chemistry and Chemical Engineering
Guangling College
Yangzhou University
Yangzhou 225002, Jiangsu, P. R. China
E-mail: panghuan@yzu.edu.cn

Dr. Y. Liu
Collaborative Innovation Center of Nonferrous
Metals of Henan Province
Henan Key Laboratory of High-Temperature Structural
and Functional Materials
School of Materials Science and Engineering
Henan University of Science and Technology
Luoyang, P. R. China

The ORCID identification number(s) for the author(s) of this article can be found under <https://doi.org/10.1002/sml.201902463>.

DOI: 10.1002/sml.201902463

reactions of the metal centers.^[31–34] However, most MOFs lack adequate conductivity and chemical durability when utilized directly as SCs electrode materials, and their capacitance is usually low.^[35] To enhance capability, one method is MOF micronano-crystallization: reducing the particle size to the micro/nanometer scale could lead to a significant decrease in the path of electrolyte ion diffusion and an increasing specific surface area of the active materials. The electrochemical properties would obviously be enhanced hence.^[36,37] Yaghi's team reported the synthesis of diverse MOF nanocrystals and found that zirconium MOF possessed fairly nice areal capacitance (5.09 mF cm⁻²) in SCs.^[38] Through great efforts, Wang and coworkers have proven that PANI-ZIF-67-CC in KCl electrolyte has a high specificity of 2,146 mF cm⁻² capacitance at 10 mV s⁻¹.^[39]

Inspired by the pioneering work of the predecessors and considering the fact that applying MOF directly to SCs electrode material is still difficult. In this work, we report the facile synthesis of hexagonal [Ni(HBTC)(4,4'-bipy)] (HBTC = 1,3,5-benzenetricarboxylic acid, 4,4'-bipy = 4,4'-bipyridine) materials with good hexagonal morphology (denoted by Ni-MOF). The largest exposed face (001) crystal plane could shorten the path of ion diffusion and electron transport. Moreover, cross-linked network structures grown on the (001) crystal plane are easily mixed with the conductive carbon to form a shorter electron transport length. At the same time, this structure forms a large number of pores, ensuring a large ionic contact surface and increasing the number of electroactive sites. In view of this structural advantage, we subsequently studied the electrochemical properties of the obtained Ni-MOF by conventional three-electrode cell. Hexagonal Ni-MOF electrode showed a specific capacitance of 977.04 F g⁻¹ at 0.5 A g⁻¹ in a 3.0 M KOH solution. In cyclic performance testing, when current density is 0.5 A g⁻¹, specific capacitance remains at 92.34% after 5000 cycles. More importantly, hexagonal Ni-MOF and AC were utilized as the positive and negative materials, respectively, to assemble aqueous devices. It was found that the aqueous devices revealed a capacitance of 189.23 F g⁻¹ at a current density of 0.5 A g⁻¹, great cycling stability, as well as high energy density.

2. Results and Discussion

Hexagonal Ni-MOF ([Ni(HBTC)(4,4'-bipy)]) was synthesized via a one-pot hydrothermal method using nickel nitrate hexahydrate as the metal source with H₃BTC and 4,4'-bipy as the organic ligand and the solvent of DMF. The MOF was synthesized by controlling reaction temperature and time to explore its growth process, and its electrochemical properties of supercapacitors were studied.

The morphologies at different magnifications of as-synthesized Y1-5 were examined by scanning electron microscopy (SEM). In **Figure 1**, a1–e1 are low-magnification SEM images at a solvothermal temperature of 80 °C and solvothermal times of 6, 12, 18, 24, and 30 h, respectively. It can be clearly seen that obtained Ni-MOF is a typical six-square structure. **Figure 1a2–e2** displays a corresponding further enlarged single hexagonal Ni-MOF with an average thickness of ≈1 μm. High-resolution transmission electron microscopy

images (**Figure S1**, Supporting Information) confirm the fact that the resulting product structure is of a certain thickness. After further enlargement, we found that a cross-linked mesh structure appeared on the surface of the hexagonal Ni-MOF (**Figure 1a3–e3**). With the extension of solvothermal time, the mesh structure gradually appeared from vagueness to clarity, then back to vagueness, and finally disappeared. The surfaces of the six squares gradually changed from smooth to rough to smooth. Compared with the other four reaction time samples, the Ni-MOF morphology obtained at 18 h (Y3) is relatively complete and uniform, and the mesh structure on the surface of the six squares is the clearest. Based on its special surface-grown mesh structures, its growth process was explored. Through reducing the amount of reactants, the samples were synthesized at 80 °C for 18 h and characterized by SEM. As shown in **Scheme S1** (Supporting Information), when the amount of the reactant is 0.375 mmol, the obtained products are piled up in sheet-like structures and initially have a hexagonal shape. By doubling the amount (0.75 mmol), the original sheet-like structures gradually accumulate into a hexagon, and the surface presents the closely packed mesh structures. Doubling the amount again (1.5 mmol), the products form a clear hexagonal shape and the dense surface mesh structures. Therefore, it is found that whole growth process is the accumulation of sheet-like structures via controlling the amount of reactants. The elemental mapping in **Figure S2** (Supporting Information) demonstrates that C, N, O, and Ni are dispersed homogeneously in Ni-MOF (Y3). Meanwhile, to further ascertain the detailed elemental composition, X-ray photoelectron spectroscopy (XPS) analysis was performed (**Figure S3**, Supporting Information). The XPS survey spectrum exhibits that hexagonal Ni-MOF consists primarily of Ni, C, N, and O elements, unambiguously confirming the existence of all elements. Six peaks are perceived in the Ni 2p spectrum (**Figure S4**, Supporting Information). There are two main spin orbital peaks: one at 872.8 eV and the other at 855.3 eV, with a spin energy separation of 17.5 eV, corresponding to Ni 2p_{1/2} and Ni 2p_{3/2}, respectively, which is a feature of Ni²⁺. The two peaks located at 881.1 and 863.23 eV correspond to Ni 2p_{1/2} and Ni 2p_{3/2} satellites, respectively. These results verify presence of Ni²⁺ in Ni-MOF, consistent with the previous literature reports.^[40,41] The peaks of Ni 2p_{1/2} and Ni 2p_{3/2} spin orbitals located at 877.63 and 859.84 eV, respectively, correspond to Ni³⁺. It can be found that the peak area of Ni²⁺ is significantly larger than that of Ni³⁺, which indicates that the Ni elements in hexagonal Ni-MOF mainly exist in the form of Ni²⁺. Moreover, we attempted to determine the effect of temperature on the morphology: the fixed reaction time was 18 h, the reaction temperature was changed to 40, 60, 80, 100 °C, and the other conditions were equal. The corresponding SEM images were shown in **Figure S5a–d** (Supporting Information). It could be found that of the four temperatures, 80 °C is the optimum temperature for the synthesis of hexagonal Ni-MOF. In order to further prove the optimal reaction condition (80 °C, 18 h) of hexagonal Ni-MOF, the morphology of obtained samples under other reaction times was continuously explored at these four temperature. As shown in **Figure S6** in the Supporting Information, it is found that the hexagonal morphology of the samples is incomplete at low temperature (40, 60 °C). As time goes

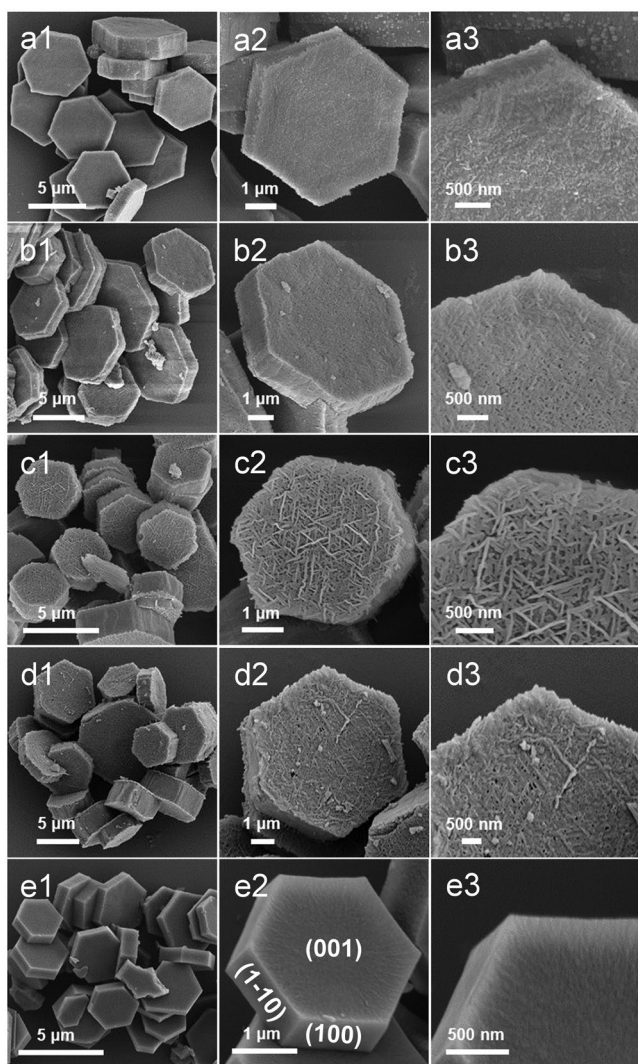


Figure 1. SEM images of hexagonal Ni-MOF obtained at varied solvothermal time at 80 °C: (a1-3) 6 h, (b1-3) 12 h, (c1-3) 18 h, (d1-3) 24 h, (e1-3) 30 h.

on, the changes of hexagonal surface mesh structures are not obvious or even no mesh structures. At high temperature (100 °C), the samples are partially damaged, and the size becomes large and uneven.

The crystal structures of obtained hexagonal Ni-MOF were further investigated by X-ray diffraction (XRD) in Figure 2a, where Y1-5 are XRD patterns of five different reaction times (6, 12, 18, 24, 30 h) at a solvothermal temperature of 80 °C. The obtained results are consistent with the previously reported (Ni(HBTC)(4,4'-bipy)),^[42] indicating that the five hexagonal Ni-MOF samples are materials with the same crystal structure. Figure 2b is a view of the structures along *ab*-axis. These hexagonal Ni-MOFs have 3D porous pillared-layer framework structures. The 2D layer consists of the central metal ion Ni (II) and partially deprotonated H₃BTC, which are then connected by a 4,4'-bipy ligand as columns along the *c*-axis between these layers to form a 3D highly porous framework (Figure 2b inset). The crystallographic planes corresponding

to (001), (002), and (003) have three distinct diffraction peaks of 7.62°, 15.59°, and 23.62°, respectively. The exposed (001) crystal plane corresponding to the hexagonal face is conducive to strong diffraction peaks of the (001), (002), and (003) crystal planes. Combined with morphology of the hexagonal Ni-MOF, as shown in the schematic diagram (Figure 2c), the top and bottom hexagonal crystal planes correspond to the (001) crystal plane, and the rectangular crystal planes correspond to (100), (1-10), and (010) crystal planes. The maximum exposure surface of (001) is a perfect structure for electron transport and electrolyte solution diffusion. The interlinked 4,4'-bipy-nickel chains provide a conductive path for the electrons on a plane perpendicular to (001). Moreover, the cross-linked porous mesh structures growing on the (001) crystal plane facilitate the storage and diffusion of electrolyte solutions, which may have excellent electrochemical properties as electrodes in supercapacitors. In short, the XRD patterns match the SEM images well. In addition, it can be seen that the patterns of Y1 and Y2 are slightly rough, with low crystallinity and poor crystal form, which may be due to the short solvothermal time. With prolonging solvothermal time, the peaks in the Y3-5 patterns are intense and sharp, indicating that the samples have high crystallinity and relatively stable crystal form. The formation of hexagonal Ni-MOF was further confirmed by performing Fourier transform-infrared radiation (FT-IR) spectroscopy. As shown in Figure 2d, the same FT-IR band of the five samples confirmed that the hexagonal Ni-MOF retained the same functional groups. From the strong absorbed peaks at 1610, 1549, and 1434 cm⁻¹, it was inferred that there is a benzene ring skeleton vibration (C=C) in the MOF. In addition, the absorption peak caused by the C-H out-of-plane bending vibration at 764 cm⁻¹ and overtone peak at 1717 cm⁻¹ further bore out the presence of the benzene ring. Signals at 815 and 717 cm⁻¹ correspond to 1,3,5 trisubstituted peaks on the benzene ring. The strong peak of carboxylate (COO⁻) was observed at 1365 cm⁻¹. C-O stretching vibrations at 1221 and 1261 cm⁻¹ also confirmed the carboxylic acids.

In a three-electrode test system, the electrochemical performance of bare Ni-foam electrode was evaluated via exploiting Pt as counter electrode and Hg/HgO as reference electrode. As shown in the Figure S7 in the Supporting Information, the bare electrode is charged and discharged rapidly under the voltage window of 0.49 V. At the current density of 0.5 A g⁻¹, the specific capacitance is only 15.23 F g⁻¹. Next, the hexagonal Ni-MOF (Y1-5) were fabricated into electrodes and a series of electrochemical performance tests were carried out in the three-electrode cell. Cyclic voltammogram (CV) curves of corresponding voltage window ranges of the five samples (Y1-5) were accomplished at 20 mV s⁻¹ to explore the suitable potential windows (Figure S8, Supporting Information). Figure 3a and Figure S9 (Supporting Information) represent CV curves of Y3 and the other four materials from 5 to 100 mV s⁻¹, respectively. These CV curves all clearly show a pair of redox peaks, indicating Faraday behavior based on the hexagonal Ni-MOF electrodes. Such faradaic features were produced by the surface redox reaction of the electrode during the electrochemical experiment. Additionally, the two redox peaks may be explained by the redox reaction of Ni(II) to Ni(III) on the surface. A similar process has been proposed for explaining the redox

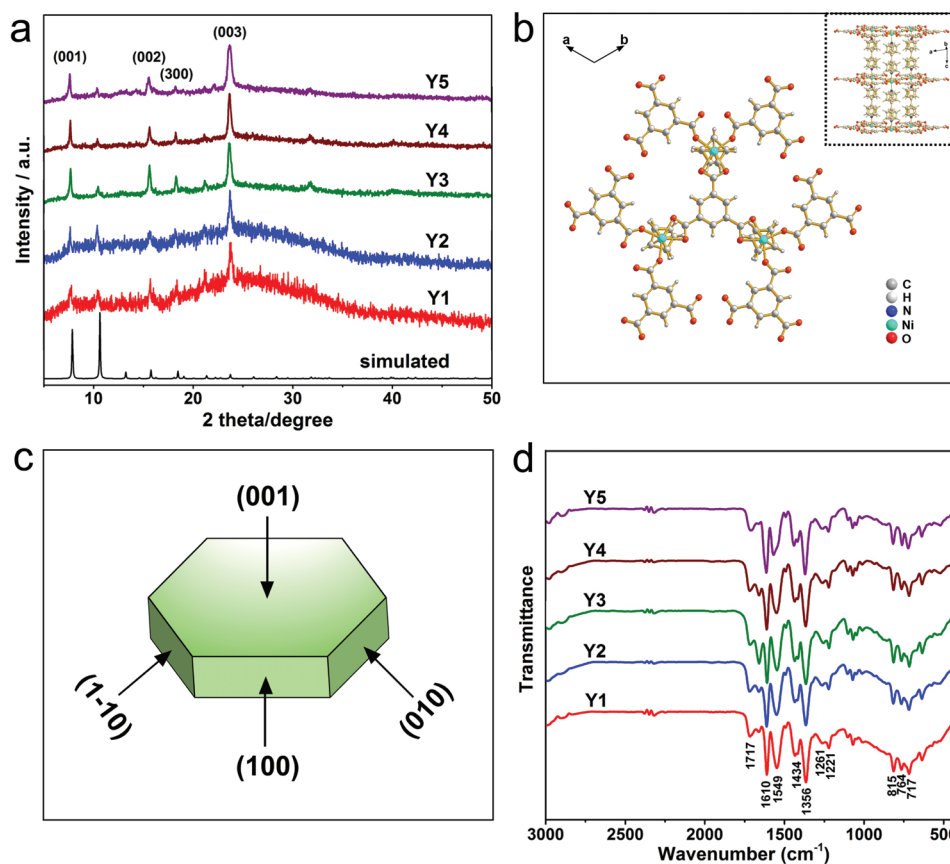
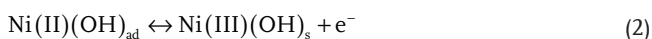
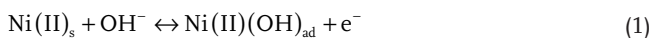


Figure 2. a) XRD patterns of the sample Y1-5. b) View of structures of hexagonal Ni-MOF 2D layer along *ab*-axis. Over the upper right corner, a view of structure perpendicular to the 2D layer. c) Schematic view of a single crystal structure of hexagonal Ni-MOF. d) FT-IR spectra of the sample Y1-5.

reaction of Ni-based MOF ($[\text{Ni}_3(\text{OH})_2(\text{C}_8\text{H}_4\text{O}_4)_2(\text{H}_2\text{O})_4] \cdot 2\text{H}_2\text{O}$ and $\text{Ni}_3(\text{btc})_2 \cdot 12\text{H}_2\text{O}$) materials.^[43] Thus, the charge-storage mechanism may be probably described as the following redox reactions given in Equations (1) and (2)



With the scanning speed increasing, curve area and peak current continue to increase, exhibiting good capacitive behavior and charge storage characteristics.

Galvanostatic charge–discharge (GCD) curves of Y1-5 electrodes at 0.5 A g^{-1} are shown in Figure 3b. The shapes of curves present characteristics of pseudocapacitance, which is consistent with CV. The corresponding specific capacitance values are calculated as 582.93, 945.65, 977.04, 825.80, and 542.98 F g^{-1} for Y1-5, respectively. In combination with the SEM images, the clearer the mesh structures on the hexagonal surface, the higher the relative specific capacitance. Compared with the other four samples, the mesh structures grown on the surface of Y3 are the most clear and complete; they easily fully mix with conductive carbon, which is more conducive to facile electrolyte distribution through electrochemical active sites and expanding specific surface area of the active materials. Therefore, the high surface area of Y3 is more effectively used to hold

a large amount of charge, resulting in the high charge storage capacitance. The GCD studies at different current densities of 0.5, 0.6, 1, 2, 3, and 5 A g^{-1} were performed, and the corresponding GCD curves are shown in Figure 3c for Y1 and in Figure S10 (Supporting Information) for Y1, Y2, Y4, and Y5. The relationship between the calculated specific capacitance value and the current density is shown in Figure 3d. It can be observed that the specific capacitance values of Y3 are 977.04, 887.75, 788.26, 709.19, 673.48, and 612.25 F g^{-1} from 0.5 to 5 A g^{-1} , respectively, which are much higher than the other four samples. The cycling stabilities of Y1-5 were further evaluated at 0.5 A g^{-1} . As can be observed from Figure 3e, the specific capacitance of Y3 can retain 93.55% of the initial value in the first 2000 cycles, and remains at 92.34% of the initial value at the end of the 5000 cycle, indicating good cycling stability. The decay of capacitance occurs mainly before 1000 cycles, and after 5000 cycles in succession, the value of the capacitance remains at 92.34% of the initial value. The main reason for the decrease of capacitance may be that during the continuous cycle, OH^- repeatedly intercalates and deintercalates at the interface of electrode/electrolyte, resulting in the structural collapse of the hexagonal Ni-MOF and hindering the electrolyte wetting electrode. The comparison of the specific capacitance of different Ni-based MOF materials is given in Table S1 (Supporting Information), and the value of Y3 is comparable to previous studies. Figures S11 and S12 (Supporting Information) show the SEM

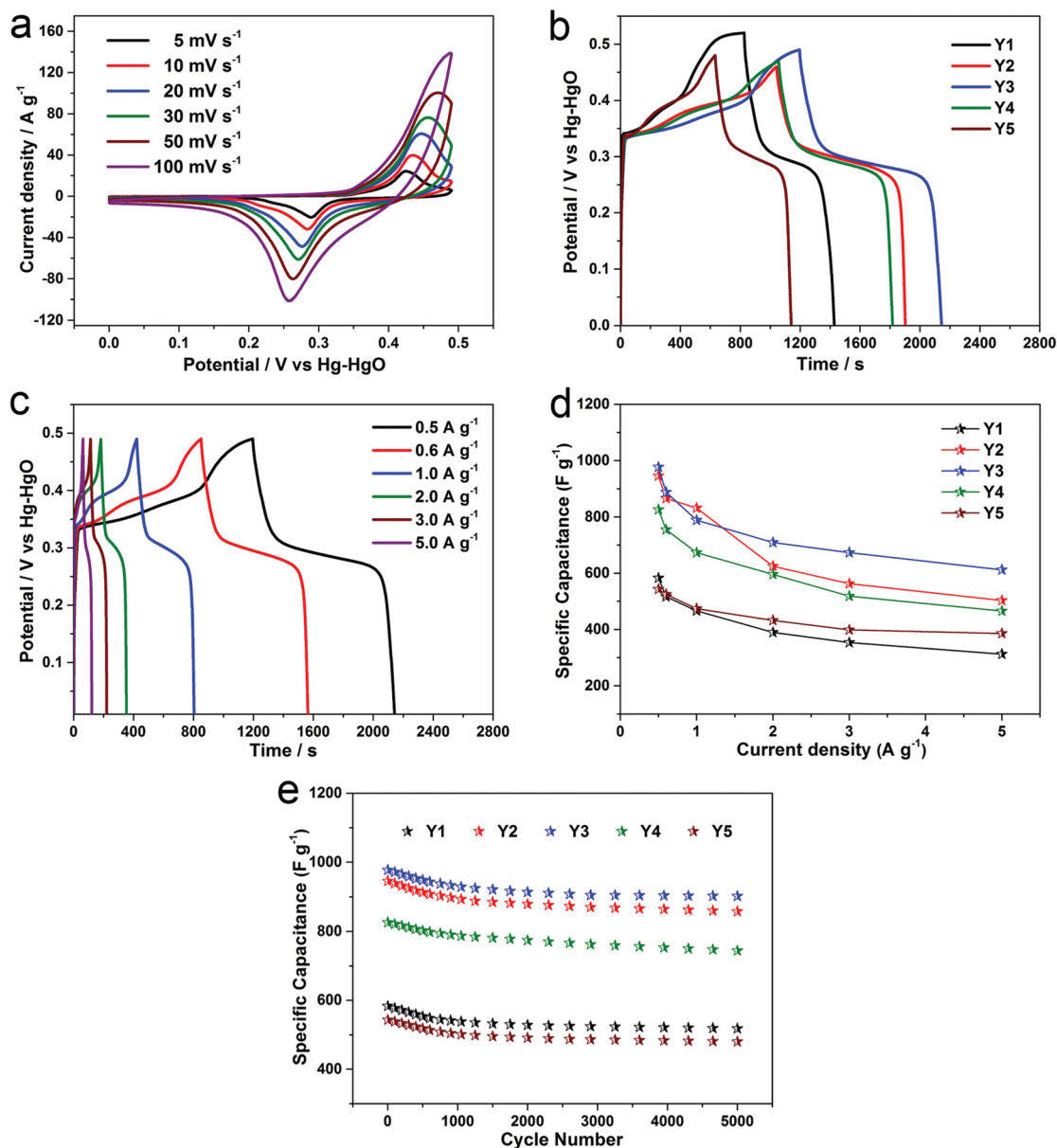


Figure 3. Electrochemical properties of as-prepared hexagonal Ni-MOF in a three-electrode cell with 3.0 M KOH aqueous solution. a) CV curves of Y3 at different scanning speeds; b) GCD curves of Y1-5 at 0.5 A g⁻¹. c) GCD curve of Y3 various current densities. d) Specific capacitance at different current densities of Y1-5. e) Cyclic performance of Y1-5 at 0.5 A g⁻¹.

and XRD patterns of Ni-MOF (Y3) after 5000 cycles using a three-electrode cell. According to the SEM image, the hexagonal Ni-MOF structures are collapsed. The XRD pattern shows that the crystal of the sample after cycling is very weak, which is quite different from the pattern before cycling. Although the Ni-MOF material has undergone some changes in the working process, it still has excellent specific capacity and good electrochemical stability. Excellent stability is important for high performance supercapacitors. To further investigate its stability, Figures S13 and S14 (Supporting Information) provide the picture, SEM and XRD patterns of Y3 after soaking in 3.0 M KOH electrolyte for 24 h. From the SEM image, the sample still maintains a hexagonal shape after soaking, and the mesh structures

on the surface disappear. XRD shows that the crystal shape after immersion becomes weak, but still has the same composition as the sample before soaking.

The electrochemical characteristics of the five samples were estimated via electrochemical impedance spectroscopy (EIS). As shown in Figure S15 (Supporting Information), the slope of Y1 is larger than the other four in the low-frequency region, implying the lower ion diffusion resistance and superior electrochemical performance of the Y3 electrode.

In order to ulteriorly study hexagonal Ni-MOF electrodes for practical applications, aqueous devices were fabricated in 3.0 M KOH with the hexagonal Ni-MOF and AC. Figure S16 (Supporting Information) shows CV curves for several voltages for

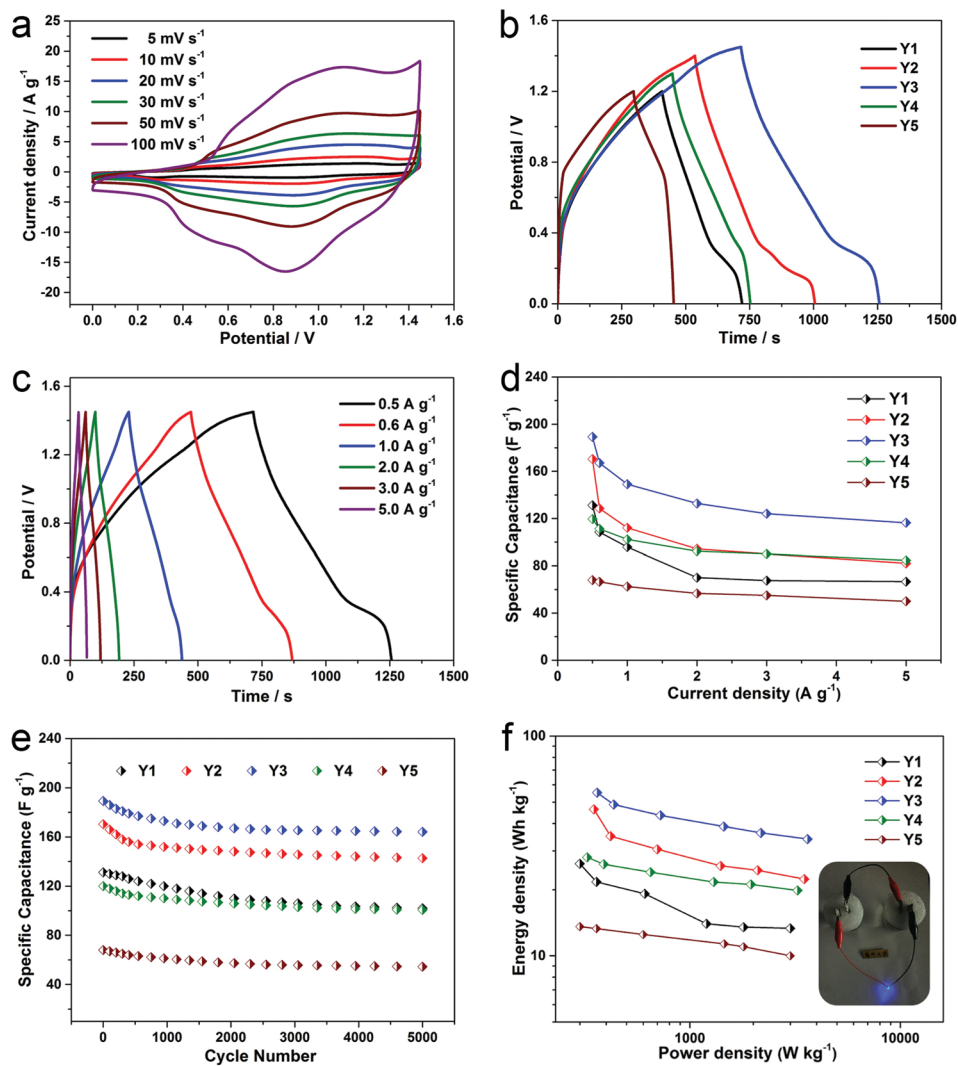


Figure 4. Electrochemical properties of as-prepared hexagonal Ni-MOF//AC aqueous devices. a) CV curves of Y3 at different scanning speeds; b) GCD curves of Y1-5 at 0.5 A g^{-1} . c) GCD curve of Y3 various current densities. d) Specific capacitance at different current densities of Y1-5. e) Cyclic capacitance of Y1-5 at 0.5 A g^{-1} . f) Ragone plot of the hexagonal Ni-MOF//AC aqueous device exhibiting the relationship between energy density and power density (inset: a blue LED powered by two series-wound aqueous devices).

hexagonal Ni-MOF//AC aqueous devices at 20 mV s^{-1} . All of them reveal pseudocapacitive behavior. GCD curves from 0.8 to 1.5 V at 0.5 A g^{-1} were measured (Figure S17, Supporting Information) to further procure opportune charge–discharge voltage values. **Figure 4a** and Figure S18 (Supporting Information) present the CV curves from 5 to 100 mV s^{-1} . It is obvious that the CV curve remains well-shaped at the sweep speed of 100 mV s^{-1} , suggesting that aqueous devices have excellent rate performance.

The GCD curves of Y1-5//AC aqueous devices with current density of 0.5 A g^{-1} are presented in Figure 4b. Corresponding specific capacitance values are 131.25, 170.36, 189.23, 119.62, and 67.92 F g^{-1} . Compared with the other four samples, the specific capacitance of Y3 is 189.23 F g^{-1} , which is the largest and is in agreement with CV. The GCD curves across a range of current densities ($0.5, 0.6, 1, 2, 3,$ and 5 A g^{-1}) are displayed in Figure 4c and Figure S19 (Supporting Information). The shapes of all charge and discharge curves are tightly linear and exhibit

a typical triangular symmetric distribution. Among them, the calculated specific capacitance values of the Y3//AC aqueous device are 189.23, 167.08, 149.14, 132.76, 124.14, and 116.38 F g^{-1} , respectively (Figure 4d), which are higher than the other four groups. Moreover, the cyclic stabilities are evaluated (Figure 4e). Under the current density of 0.5 A g^{-1} , the capacitance of Y3//AC changed from 189.23 to 164.20 F g^{-1} and remained at 86.77% after 5000 charging and discharging cycles. At the open circuit voltage, EIS spectra (Figure S20, Supporting Information) were measured to ascertain their small charge transfer resistance. Beyond dispute, Y3 is the smallest. To investigate the overall properties of hexagonal Ni-MOF//AC aqueous devices, Ragone plots are drawn in Figure 4f from GCD curves based on their two-electrode system. The Ragone plots demonstrate the relationship between energy density and power density for five different aqueous devices. It can be found that the hexagonal Ni-MOF (Y3)//AC manifests a high energy density of 55.26 Wh kg^{-1}

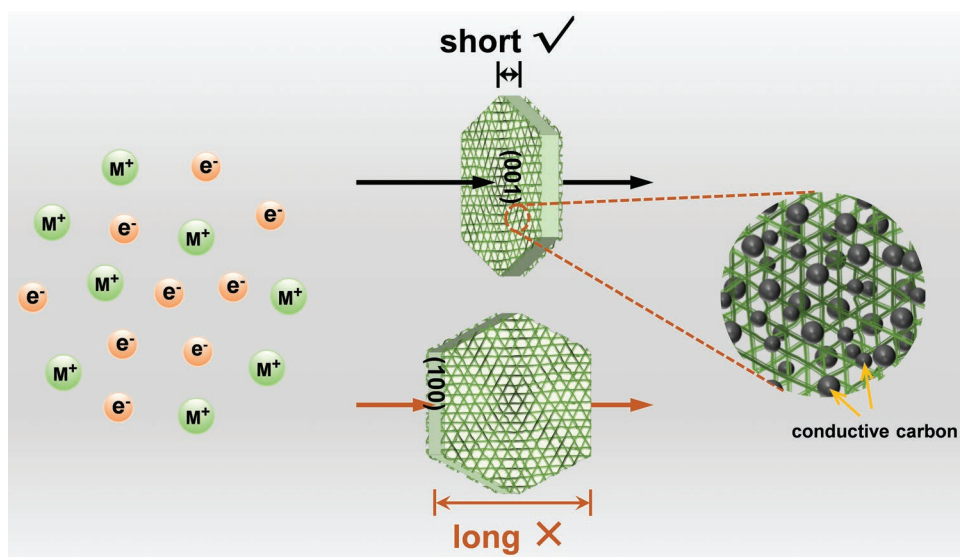


Figure 5. Schematic diagram of charge transfer process on (001) and rectangular crystal planes, respectively.

at a power density of 362.50 W kg^{-1} and maintains a value of 33.98 Wh kg^{-1} under $3624.87 \text{ W kg}^{-1}$, and its splendid rate performance is distinctly higher than those of the other four devices. Meanwhile, the Ni-MOF (Y3)//AC device performs well compared to the similar materials that have been reported recently (Figure S21, Supporting Information), such as $\text{Ni}_3(\text{btc})_2 \cdot 12\text{H}_2\text{O}$ //AC (16.5 Wh kg^{-1}), Ni-MOF//AC ASCs (21.05 Wh kg^{-1}), and GM-LEG@Ni-MOF//AC ASC (32.7 Wh kg^{-1}). To demonstrate that the device can be employed in practical application, the aqueous device was used to power a blue light-emitting diode (LED), which is presented in the inset of Figure 4f.

In this present work, hexagonal Ni-MOF can be successfully applied to SCs electrode materials with outstanding properties including large capacitance, good rate performance and excellent cycle stability. First, the materials offer a 3D porous layer framework structure. Large layer spacing is beneficial for electrolyte diffusion and OH^- intercalation/deintercalation. Second, the exposed (001) crystal plane shortens the path of electron transport and ion diffusion. As shown in Figure 5, when electrons and ions pass through the electrode materials, the length of passing through the (001) crystal plane is noticeably shorter than the surrounding rectangular crystal plane. The transportation path is shortened, the transportation rate is accelerated, and the electrochemical performance is improved. Finally, the cross-linked mesh structures growing on the (001) crystal plane enhances mixing with the conductive carbon, causing the electrode materials to become more conductive and accelerating electron transfer at the electrode–electrolyte interface. Simultaneously, mesh structures could increase the ion contact area and expose more active sites. In this instance, it would be easier for substrate molecules to interact with the active site and further improve the electrical properties.

3. Conclusions

In conclusion, we have designed and prepared the hexagonal Ni-MOF materials using a controllable one-step solvothermal

method. The electrochemical performance of hexagonal Ni-MOF was investigated via a three-electrode cell and aqueous device. In a three-electrode cell, sample Y3 electrode displayed a maximum specific capacitance of 977.04 F g^{-1} at 0.5 A g^{-1} , and held 92.34% of the initial value after 5000 cycles. More importantly, the Y3//AC aqueous device possesses specific capacitance of 189.23 F g^{-1} at 0.5 A g^{-1} . The preeminent electrochemical performance could be ascribed to essential features of the hexagonal Ni-MOF, such as favorable {001} exposed facets and the surface-grown cross-linked mesh structures. Ni-based MOF materials have extensively served as SCs electrode materials. However, as MOF materials, the hexagonal Ni-MOF has the disadvantage of poor electrical conductivity. Combining MOFs with highly conductive materials involving carbon nanotubes, graphenes, and conductive polymers represents a promising future research trend.

Supporting Information

Supporting Information is available from the Wiley Online Library or from the author.

Acknowledgements

This work was supported by the National Natural Science Foundation of China (NSFC-21671170, 21673203, and 21201010), the Top-notch Academic Programs Project of Jiangsu Higher Education Institutions (TAPP), Program for New Century Excellent Talents of the University in China (NCET-13-0645), the Six Talent Plan (2015-XCL-030), and Qinglan Project. The authors also acknowledge the Priority Academic Program Development of Jiangsu Higher Education Institutions and the technical support we received at the Testing Center of Yangzhou University.

Conflict of Interest

The authors declare no conflict of interest.

Keywords

cross-linked mesh structures, exposing crystal plane, hexagonal Ni-MoF, supercapacitors

Received: May 14, 2019
Revised: June 18, 2019
Published online:

- [1] X. Wang, J. Zhuang, Q. Peng, Y. Li, *Nature* **2005**, 437, 121.
- [2] S. Sun, C. B. Murray, D. Weller, L. Folks, A. Moser, *Science* **2000**, 287, 1989.
- [3] D. M. Vriezema, M. C. Aragone, J. A. A. W. Elemans, J. J. L. M. Cornelissen, A. E. Rowan, R. J. M. Nolte, *Chem. Rev.* **2005**, 105, 1445.
- [4] B. Li, N. You, Y. Liang, Q. Zhang, W. Zhang, M. Chen, X. Pang, *Energy Environ. Mater.* **2019**, 2, 38.
- [5] S.-L. Li, Q. Xu, *Energy Environ. Sci.* **2013**, 6, 1656.
- [6] G. Li, S. Zhao, Y. Zhang, Z. Tang, *Adv. Mater.* **2018**, 30, 1800702.
- [7] L. Wang, Y. Han, X. Feng, J. Zhou, P. Qi, B. Wang, *Coord. Chem. Rev.* **2016**, 307, 361.
- [8] H. Furukawa, K. E. Cordova, M. O'Keeffe, O. M. Yaghi, *Science* **2013**, 341, 1230444.
- [9] J. P. Zhang, Y. B. Zhang, J. B. Lin, X. M. Chen, *Chem. Rev.* **2012**, 112, 1001.
- [10] B. Chen, S. Xiang, G. Qian, *Acc. Chem. Res.* **2010**, 43, 1115.
- [11] B. Li, H. M. Wen, Y. Cui, W. Zhou, G. Qian, B. Chen, *Adv. Mater.* **2016**, 28, 8819.
- [12] a) Z. Zhang, Z. Z. Yao, S. Xiang, B. Chen, *Energy Environ. Sci.* **2014**, 7, 2868; b) D.-M. Chen, J.-Y. Tian, C.-S. Liu, M. Du, *Chem. Commun.* **2016**, 52, 8413.
- [13] J.-R. Li, J. Sculley, H.-C. Zhou, *Chem. Rev.* **2012**, 112, 869.
- [14] a) Y. Xu, B. Li, S. Zheng, P. Wu, J. Zhan, H. Xue, Q. Xu, H. Pang, *J. Mater. Chem. A* **2018**, 6, 22070; b) D. Shi, R. Zheng, M.-J. Sun, X. Cao, C.-X. Sun, C.-J. Cui, C.-S. Liu, J. Zhao, M. Du, *Angew. Chem.-Int. Ed.* **2017**, 56, 14637.
- [15] W. Xia, A. Mahmood, R. Zou, Q. Xu, *Energy Environ. Sci.* **2015**, 8, 1837.
- [16] a) Y. Guo, X. Feng, T. Han, S. Wang, Z. Lin, Y. Dong, B. Wang, *J. Am. Chem. Soc.* **2014**, 136, 15485; b) M. Chen, W.-M. Xu, J.-Y. Tian, H. Cui, J.-X. Zhang, C.-S. Liu, M. Du, *J. Mater. Chem. C* **2017**, 5, 2015.
- [17] F. S. Ke, Y. S. Wu, H. Deng, *J. Solid State Chem.* **2015**, 223, 109.
- [18] X. Wu, W. Deng, J. Qian, Y. Cao, X. Ai, H. Yang, *J. Mater. Chem. A* **2013**, 1, 10130.
- [19] a) Y. Zhang, S. Yuan, X. Feng, H. Li, J. Zhou, B. Wang, *J. Am. Chem. Soc.* **2016**, 138, 5785; b) F. Wang, Y. Liu, Y. F. Zhao, Y. Wang, Z. J. Wang, W. H. Zhang, F. Z. Ren, *Appl. Sci.* **2018**, 8, 22.
- [20] a) C. Qu, Y. Jiao, B. Zhao, D. Chen, R. Zou, K. S. Walton, M. Liu, *Nano Energy* **2016**, 26, 66; b) Y. Liu, X. Zhai, K. Yang, F. Wang, H. Wei, W. Zhang, F. Ren, H. Pang, *Front. Chem.* **2019**, 7, 118.
- [21] Y. Li, Y. Xu, W. Yang, W. Shen, H. Xue, H. Pang, *Small* **2018**, 14, 1704435.
- [22] W. Yang, X. Li, Y. Li, R. Zhu, H. Pang, *Adv. Mater.* **2019**, 31, 1804740.
- [23] L. Shen, J. Wang, G. Xu, H. Li, H. Dou, X. Zhang, *Adv. Energy Mater.* **2014**, 5, 1400977.
- [24] J. T. Mefford, W. G. Hardin, S. Dai, K. P. Johnston, K. J. Stevenson, *Nat. Mater.* **2014**, 13, 726.
- [25] J. Yang, Y. Yuan, W. Wang, H. Tang, Z. Ye, J. Lu, *J. Power Sources* **2017**, 340, 6.
- [26] H. Chen, L. Hu, M. Chen, Y. Yan, L. Wu, *Adv. Funct. Mater.* **2013**, 24, 934.
- [27] J. Kim, J. Lee, J. You, M.-S. Park, M. S. Al Hossain, Y. Yamauchi, J. H. Kim, *Mater. Horiz.* **2016**, 3, 517.
- [28] J. Yang, Z. Ma, W. Gao, M. Wei, *Chem.-Eur. J.* **2017**, 23, 631.
- [29] S. Zheng, H. Xue, H. Pang, *Coord. Chem. Rev.* **2018**, 373, 2.
- [30] S. Zheng, X. Li, B. Yan, Q. Hu, Y. Xu, X. Xiao, H. Xue, H. Pang, *Adv. Energy Mater.* **2017**, 7, 1602733.
- [31] X. Liu, C. Shi, C. Zhai, M. Cheng, Q. Liu, G. Wang, *ACS Appl. Mater. Interfaces* **2016**, 8, 4585.
- [32] J. Yang, P. Xiong, C. Zheng, H. Qiu, M. Wei, *J. Mater. Chem. A* **2014**, 2, 16640.
- [33] J. Sun, Q. Xu, *Energy Environ. Sci.* **2014**, 7, 2071.
- [34] Y. Xu, Q. Li, H. Xue, H. Pang, *Coord. Chem. Rev.* **2018**, 376, 292.
- [35] Y. Yan, P. Gu, S. Zheng, M. Zheng, H. Pang, H. Xue, *J. Mater. Chem. A* **2016**, 4, 19078.
- [36] X. Zhang, L. Chang, Z. Yang, Y. Shi, C. Long, J. Han, B. Zhang, X. Qiu, G. Li, Z. Tang, *Nano Res.* **2019**, 12, 437.
- [37] S. Zhao, Y. Wang, J. Dong, C.-T. He, H. Yin, P. An, K. Zhao, X. Zhang, C. Gao, L. Zhang, J. Lv, J. Wang, J. Zhang, A. M. Khattak, N. A. Khan, Z. Wei, J. Zhang, S. Liu, H. Zhao, Z. Tang, *Nat. Energy* **2016**, 1, 1.
- [38] K. M. Choi, H. M. Jeong, J. H. Park, Y. B. Zhang, J. K. Kang, O. M. Yaghi, *ACS Nano* **2014**, 8, 7451.
- [39] L. Wang, X. Feng, L. Ren, Q. Piao, J. Zhong, Y. Wang, H. Li, Y. Chen, B. Wang, *J. Am. Chem. Soc.* **2015**, 137, 4920.
- [40] J. Liang, R. Ma, N. Iyi, Y. Ebina, K. Takada, T. Sasaki, *Chem. Mater.* **2010**, 22, 371.
- [41] J. W. Lee, T. Ahn, D. Soundararajan, J. M. Ko, J. D. Kim, *Chem. Commun.* **2011**, 47, 6305.
- [42] C. Gao, S. Liu, L. Xie, Y. Ren, J. Cao, C. Sun, *CrystEngComm* **2007**, 9, 545.
- [43] L. Kang, S.-X. Sun, L.-B. Kong, J.-W. Lang, Y.-C. Luo, *Chin. Chem. Lett.* **2014**, 25, 957.